Supplement of Atmos. Chem. Phys., 25, 9617–9643, 2025
https://doi.org/10.5194/acp-25-9617-2025-supplement

Atmospheric Chemistry and Physics
Open Access
EGU

Supplement of

Evaluating reanalysis representations of climatological trace gas distributions in the Asian monsoon tropopause layer

Jonathon S. Wright et al.

Correspondence to: Jonathon S. Wright (jswright@tsinghua.edu.cn)

Summary

This online supplement contains nine figures that extend the analysis reported in the main text of this paper:

(1) **Figure S1–S2.** Distributions of temperature based on Aura MLS, ERA5, and ERA5.1, along with tropopause pressure based on the Atmospheric Infrared Sounder (AIRS). Fig. S2 focuses on differences between ERA5 and ERA5.1 during 2005–2006 (Fig. 2 in the main text).

(2) **Figures S3–S5.** Three-dimensional climatologies of water vapor, ozone, and carbon monoxide in the Asian monsoon tropopause layer over 1 May–2 October 2005–2021, without subtracting the zonal mean (Figures 3, 4, 5 in the main text).

(3) **Figure S6.** Global spatial distributions of time-mean May–September water vapor from Aura MLS and JRA-3Q (Figure 6 in the main text).

(4) **Figure S7.** Moistening rates due to parameterized physics in JRA-3Q showing tendencies at 121 hPa rather than 83 hPa (Figure 8 in the main text).

(5) **Figure S8.** Mean distributions of water vapor tendencies due to dynamics, physics, data assimilation, and nudging in MERRA-2.

(6) **Figure S9.** Mean seasonal cycle of water vapor volume mixing ratios at 83 hPa.

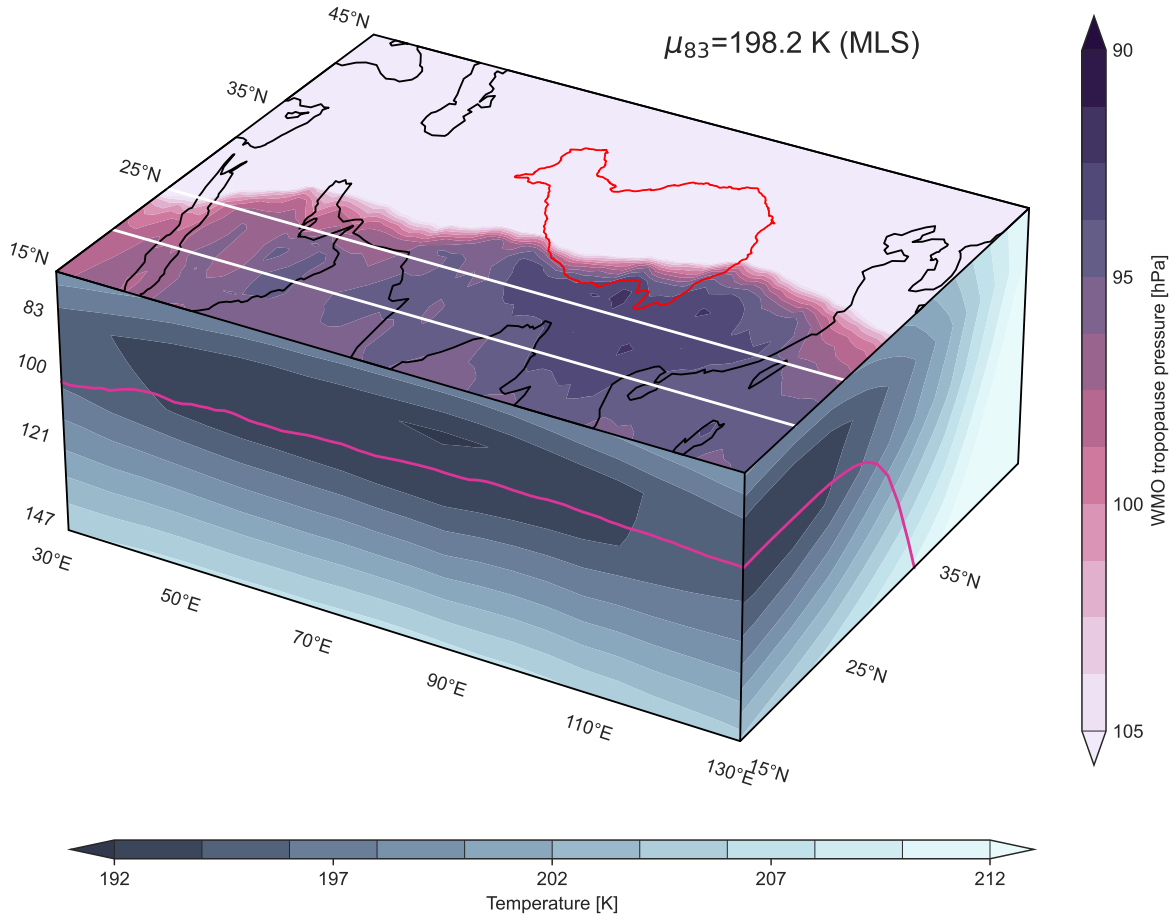

Figure S1. Mean temperature distribution for May–September 2005–2021 from Aura MLS and mean tropopause pressure for the same period from the Atmospheric Infrared Sounder (AIRS). The top face in shows the geographic distribution of tropopause pressure based on AIRS. The east (right) face shows temperature from Aura MLS averaged zonally over 30–130°E, along with the mean tropopause pressure over the same longitude range. The south (left) face shows the meridional-mean temperature from Aura MLS averaged over 20–25°N, along with the mean tropopause pressure averaged over the same latitude range.

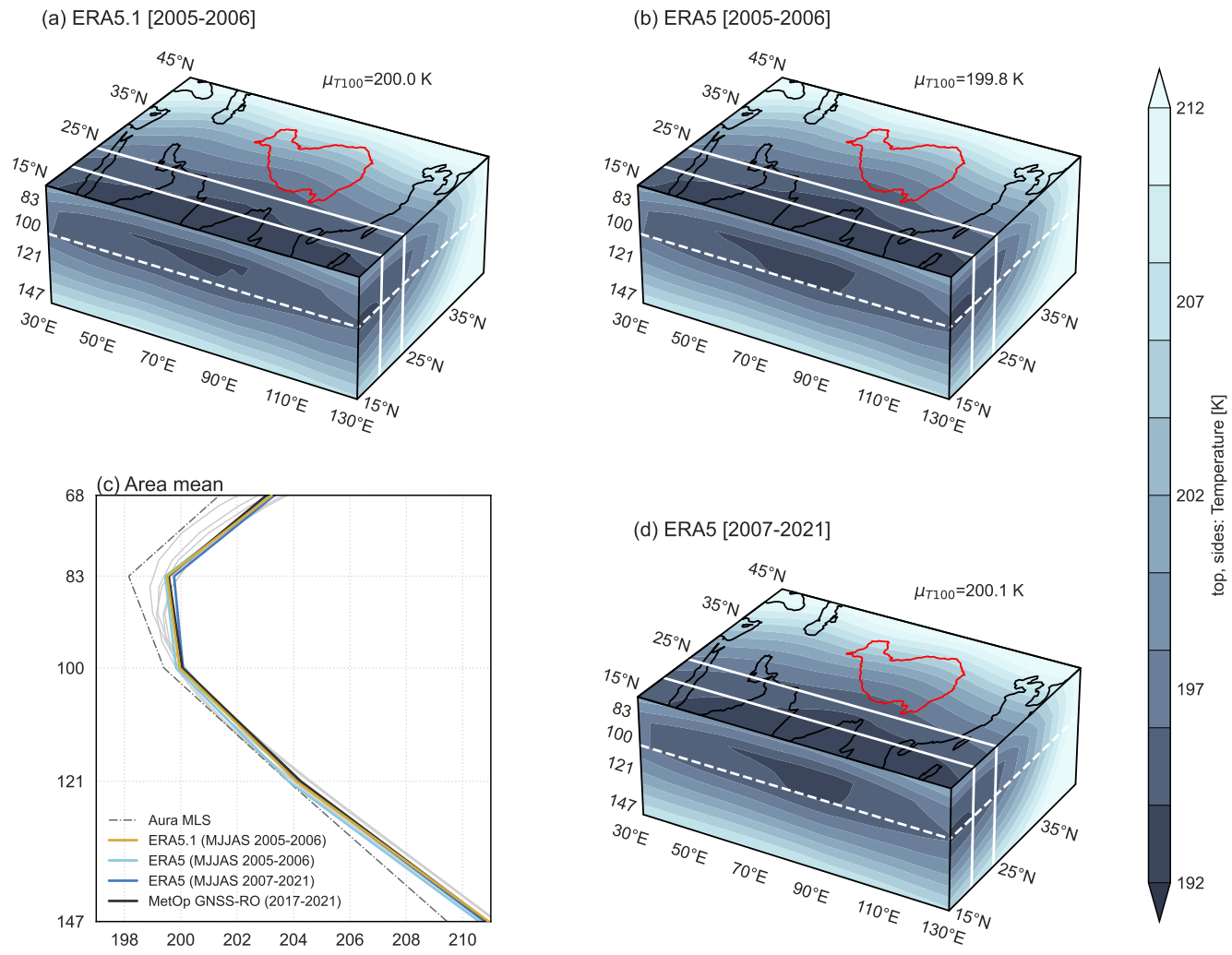

Figure S2. Mean temperature distributions for May–September from (a) ERA5.1 for 2005–2006, (b) ERA5 for 2005–2006, and (d) ERA5 for 2007–2021. Area-mean profiles (30–130°E, 15–45°N) for the same distributions are shown in (c), with profiles from Aura MLS, MetOp radio occultation, MERRA-2, and JRA-3Q also included for context. The top faces in panels (a), (b), and (d) show distributions on the 100 hPa isobaric surface, the east (right) faces show regional-mean distributions averaged over 30–130°E, and the south (left) faces show meridional-mean distributions averaged over 20–25°N. Distributions are interpolated to Aura MLS pressure levels (147 hPa, 121 hPa, 100 hPa, 83 hPa, and 68 hPa) from ERA5 and ERA5.1 model-level products. Differences between ERA5.1 and ERA5 during 2005–2006 are largest in the lower part of the layer, approaching ∼0.3 K at 147 hPa, but are generally small. Both are in good agreement with MetOp GNSS-RO during 2017–2021 and slightly colder than ERA5 for the later 2007–2021 period. Higher-resolution dry temperature profiles from MetOp GNSS-RO (light grey lines) show substantial interannual variability in the vertical location and magnitude of the cold point during 2017–2021. Interannual and intraseasonal variability in reanalysis representations of the monsoon tropopause layer will be addressed in a forthcoming follow-up paper.

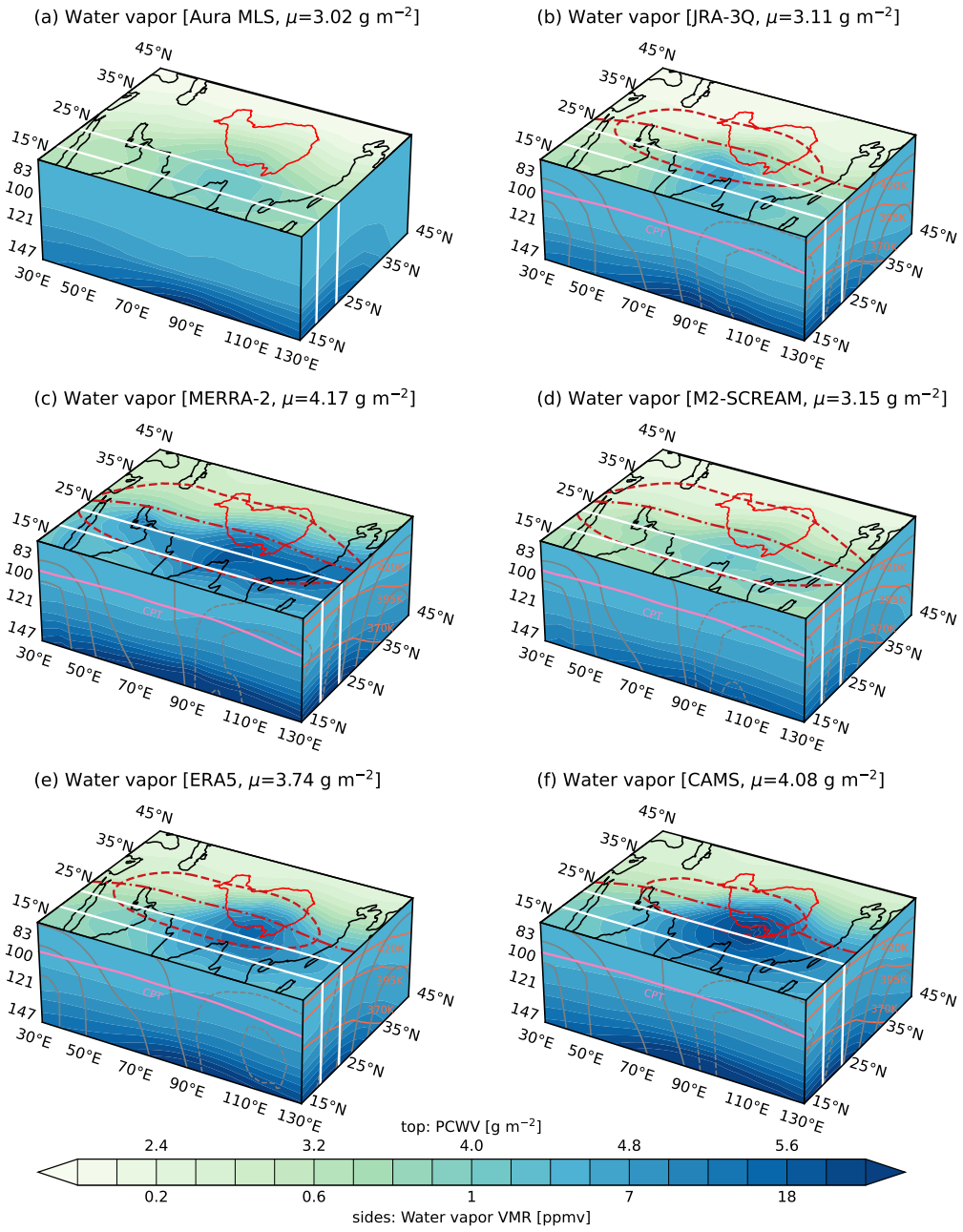

Figure S3. Climatological distributions of partial-column water vapor (PCWV; eq. 1 in the main text) integrated over the 68–147 hPa layer (top), water vapor transects averaged over 20°N–25°N (left/south side; white lines), and zonal-mean water vapor averaged over 30°E–130°E (right/east side) based on (a) Aura MLS, (b) JRA-3Q, (c) MERRA-2, (d) M2-SCREAM, (e) ERA5, and (f) CAMS during 1 May–2 October 2005–2021. The 369 200 m^2 s^{-2} contour of Montgomery streamfunction (dashed red contour) and 0 m s^{-1} zonal wind contour (dashdot red contour) are shown for the 395 K isentropic surface on the top faces of (b)–(f). The cold point tropopause (pink contour) and meridional winds (grey contours) are shown for the east–west transect on the south face, while zonal-mean potential temperature (orange contours) and zonal-mean zonal wind (gray contour) are shown on the east face. Red contours in all panels mark the location of the Tibetan Plateau. The figure corresponds to climatological anomalies of water vapor relative to the zonal mean shown as Figure 2 in the main text.

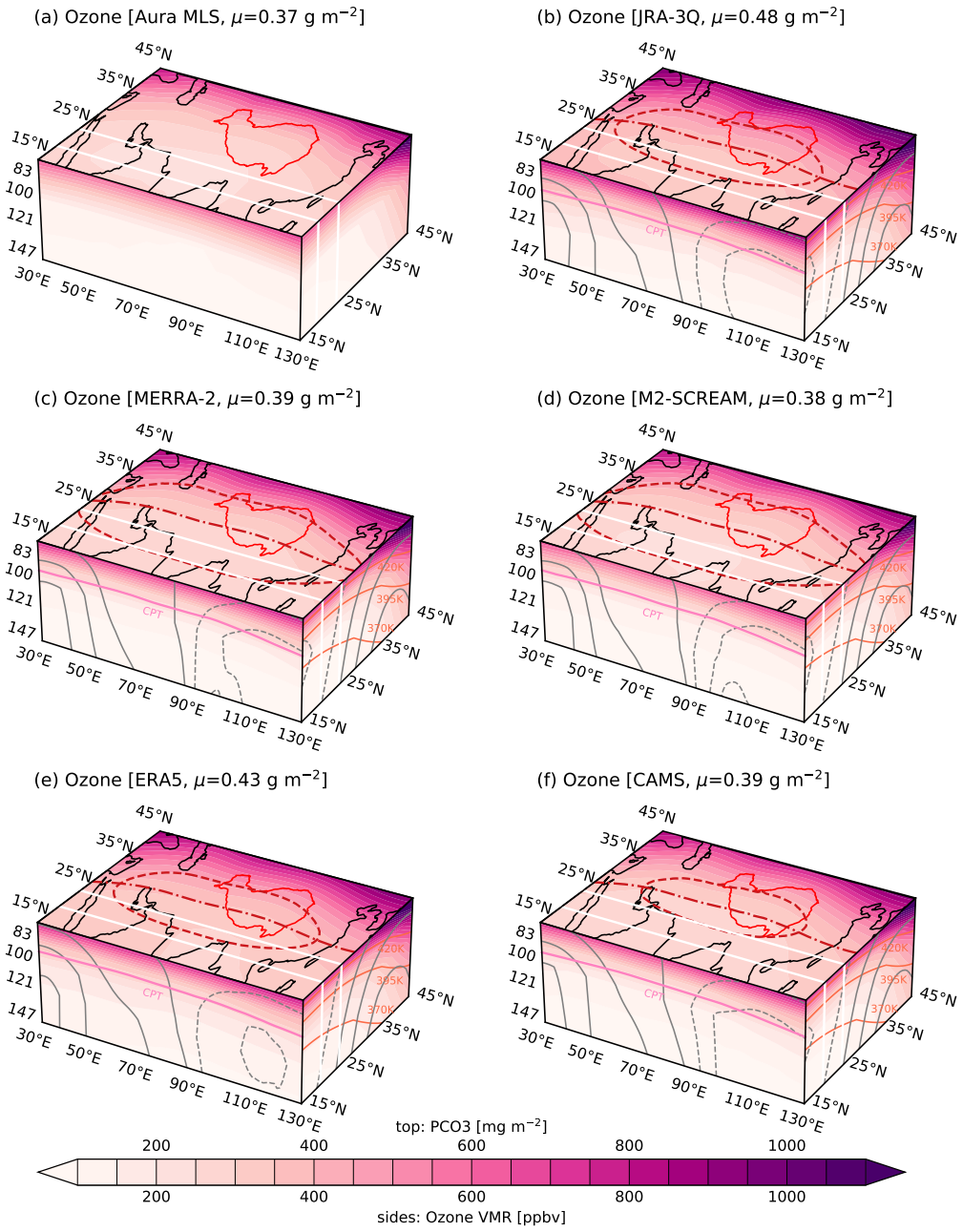

Figure S4. Climatological distributions of partial-column ozone (PCO3) integrated over the 68–147 hPa layer (top), ozone transects averaged over 20°N–25°N (left/south side; white lines), and zonal-mean ozone averaged over 30°E–130°E (right/east side) based on (a) Aura MLS, (b) JRA-3Q, (c) MERRA-2, (d) M2-SCREAM, (e) ERA5, and (f) CAMS during 1 May–2 October 2005–2021. The 369 200 m^2 s^{-2} contour of Montgomery streamfunction (dashed red contour) and 0 m s^{-1} zonal wind contour (dashdot red contour) are shown for the 395 K isentropic surface on the top faces of (b)–(f). The cold point tropopause (pink contour) and meridional winds (grey contours) are shown for the east–west transect on the south face, while zonal-mean potential temperature (orange contours) and zonal-mean zonal wind (gray contour) are shown on the east face. Red contours in all panels mark the location of the Tibetan Plateau. The figure corresponds to climatological anomalies of ozone relative to the zonal mean shown as Figure 3 in the main text.

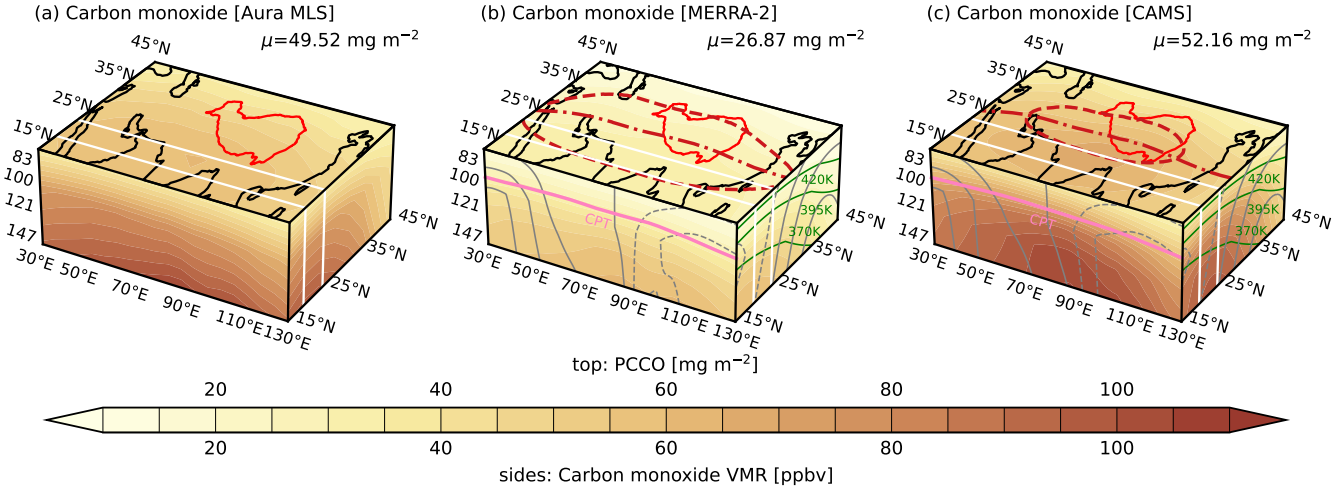

Figure S5. Climatological distributions of partial-column carbon monoxide (PCCO) integrated over the 68–147 hPa layer (top), CO transects averaged over 20°N–25°N (left/south side; white lines), and zonal-mean CO averaged over 30°E–130°E (right/east side) based on (a) Aura MLS, (b) MERRA-2, and (c) CAMS during 1 May–2 October 2005–2021. The 369 200 $m^2\,s^{-2}$ contour of Montgomery streamfunction (dashed red contour) and 0 $m\,s^{-1}$ zonal wind contour (dashdot red contour) are shown for the 395 K isentropic surface on the top face. The cold point tropopause (pink contour) and meridional winds (grey contours) are shown for the east–west transect on the south face, while zonal-mean potential temperature (orange contours) and zonal-mean zonal wind (gray contour) are shown on the east face. Red contours in all panels mark the location of the Tibetan Plateau. The figure corresponds to climatological anomalies of CO for Aura MLS, MERRA-2, and CAMS relative to the zonal mean shown as Figure 5 in the main text.

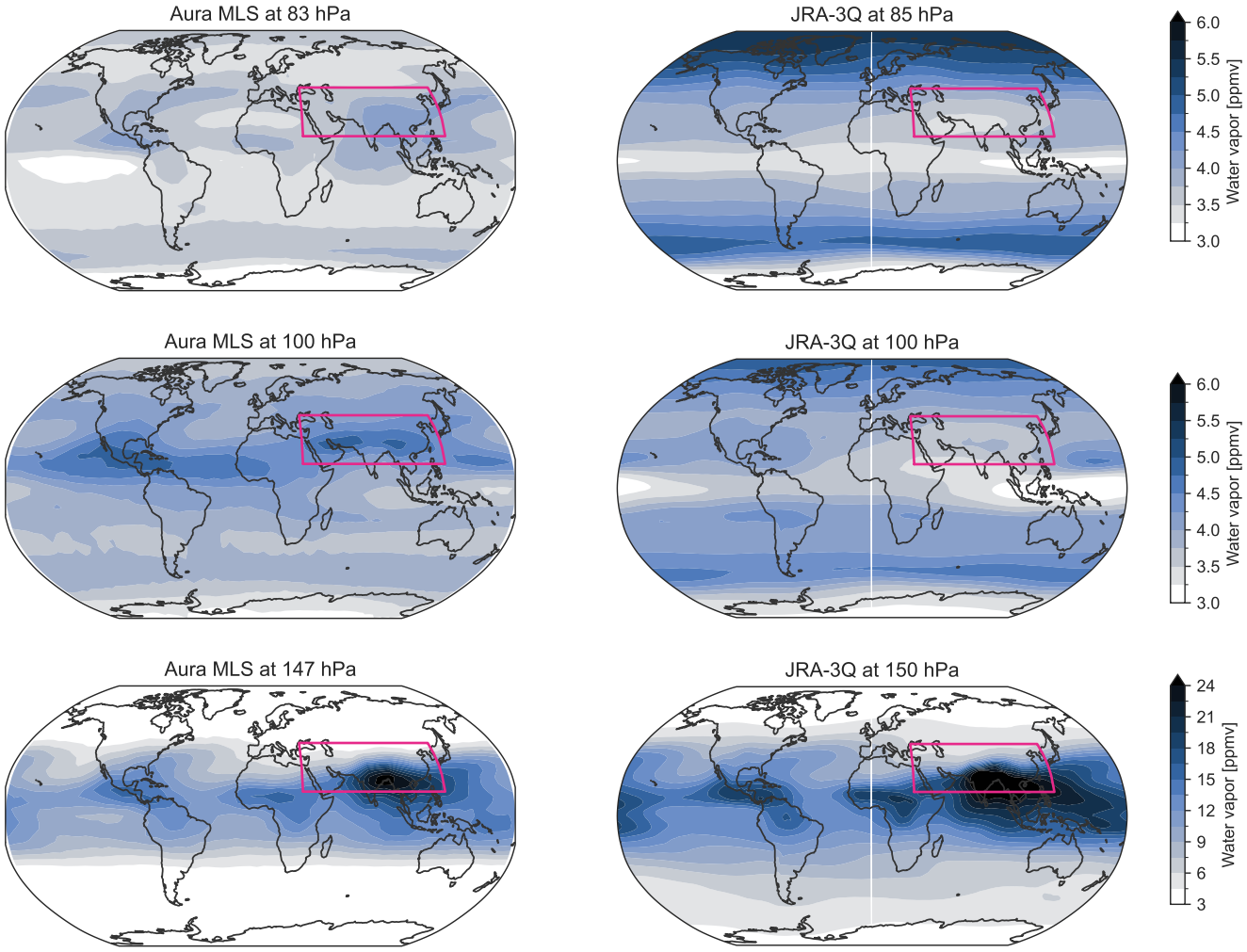

Figure S6. Spatial distributions of water vapor specific humidities during May–September 2005–2021 from (left) Aura MLS and (right) JRA-3Q at the pressure levels closest to (bottom row) 150 hPa, (middle row) 100 hPa, and (upper row) 85 hPa. These distributions show a dramatic change in the agreement with MLS in the spatial distribution of water vapor between 150 hPa, which matches well qualitatively despite an obvious moist bias, and 83 hPa, where the distribution with latitude in the Northern Hemisphere is almost opposite in JRA-3Q relative to Aura MLS. Substantial qualitative disagreements are evident for $p \leq 100$ hPa. Unlike MERRA-2 (which nudges to a climatology) or ERA5 (which disallows assimilation increments in water vapor above the tropopause), water vapor in JRA-3Q can be influenced by assimilated observations throughout the depth of the atmosphere. The relatively small mean assimilation increments in JRA-3Q water vapor (Fig. 11 in the main text) at these levels indicate that these biases build up over time. Moreover, the ability of the JRA-3Q forecast model to simulate the expected balance of processes controlling water vapor in the monsoon tropical tropopause layer (TTL) given current assimilation constraints in the troposphere (see sect. 4 of the main text) suggests that disallowing assimilation increments in water vapor above the tropopause as is done in ERA5 may well substantially improve the mismatch shown here. Stratospheric water vapor in JRA-55 suffered similar issues but with larger quantitative errors due to large increments in tropospheric water vapor influencing water vapor non-locally (Kobayashi et al. 2024); although the situation is clearly improved quantitatively in JRA-3Q, the qualitative mismatch remains.

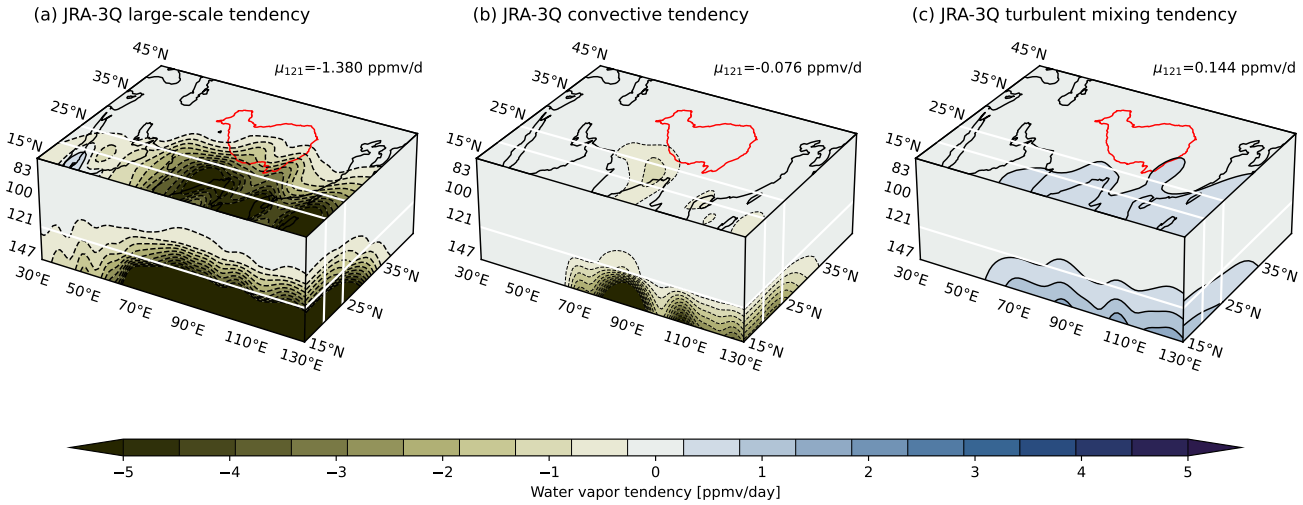

Figure S7. Water vapor tendencies from parameterized (a) large-scale cloud and precipitation processes, (b) convection, and (c) vertical turbulent diffusion based on JRA-3Q. Red contours mark the location of the Tibetan Plateau and white lines mark the boundaries of the east–west transect and the vertical location of the top face. This figure is the same as Fig. 8 in the main text except that the top face shows the distribution at 121 hPa rather than 83 hPa.

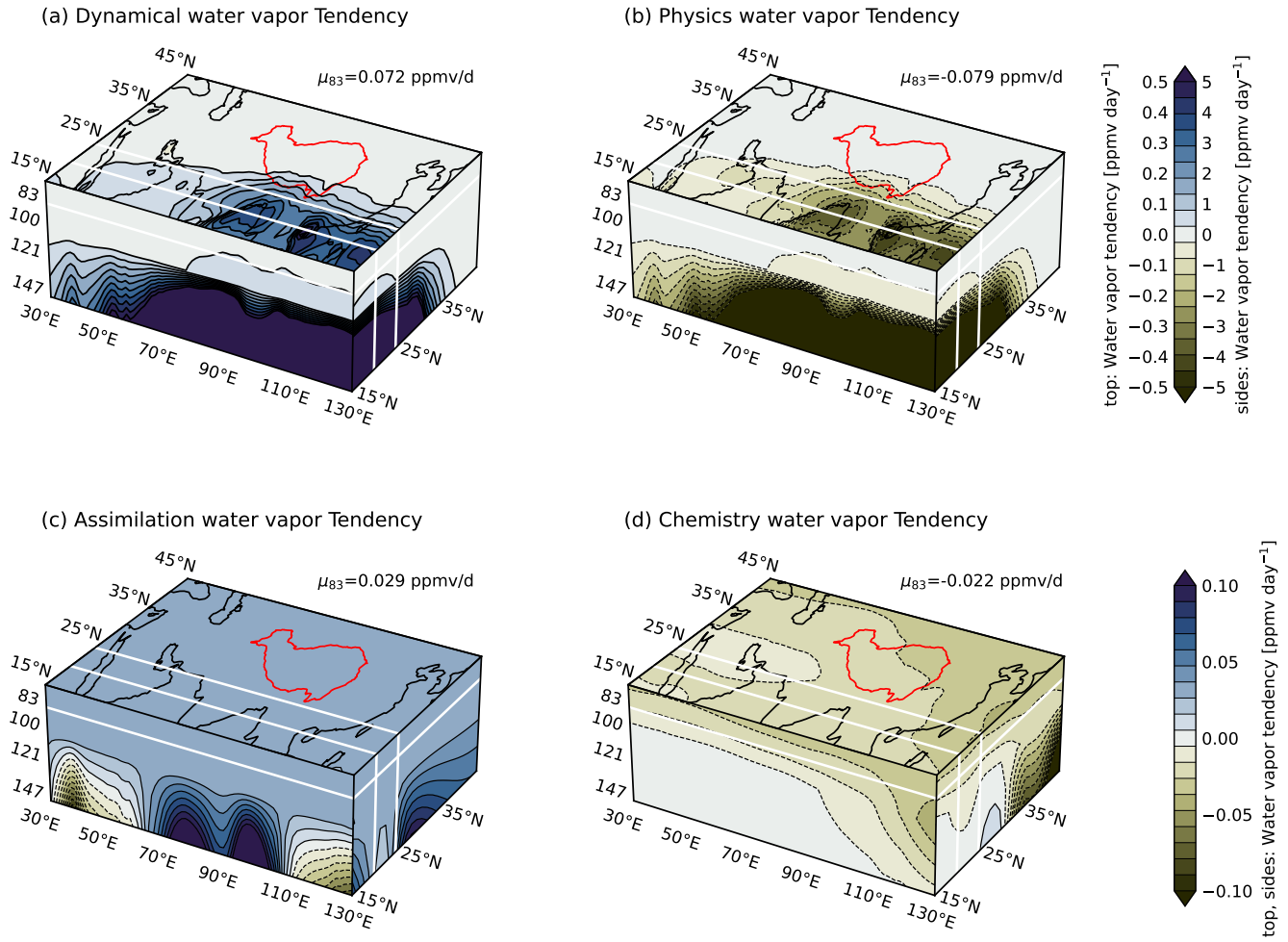

Figure S8. Water vapor tendencies from (a) dynamics, (b) parameterized physics, (c) data assimilation, and (d) nudging based on MERRA-2. The nudging term is labeled 'DQDTCHM' in the MERRA-2 'qdt' collections. Red contours mark the location of the Tibetan Plateau and white lines mark the boundaries of the east–west transect and the vertical location of the top face. Note the substantial influence of the nudging term along the eastern edge of the anticyclone (panel d), potentially related to southward stratospheric intrusions. This component is largely offset by large positive assimilation tendencies in the same region (panel c). This figure corresponds to Figures 7 and 11 in the main text.

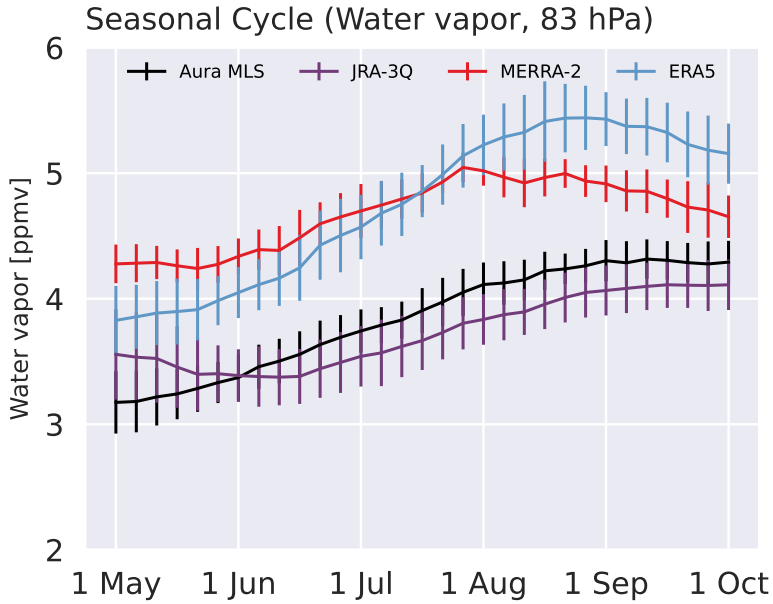

Figure S9. Seasonal cycle of water vapor mixing ratios at 83 hPa based on Aura MLS, MERRA-2, ERA5, and JRA-3Q. This figure supplements Figure 6 in the main text.